

Direct Numerical Simulation of Aerosol Growth Processes in a Turbulent Mixing Layer

Kun Zhou, Antonio Attili, and Fabrizio Bisetti

Corresponding author: kun.zhou@kaust.edu.sa

Clean Combustion Research Center, King Abdullah University of Science and Technology,
Thuwal 23955, Kingdom of Saudi Arabia

Abstract: The complex interaction of turbulent mixing and aerosol growth processes in a canonical turbulent flow configuration is investigated by means of direct numerical simulation. A cold gaseous stream mixes with a hot stream of vapor in a developing mixing layer. Nanometer sized particles (droplets) nucleate as vapor becomes supersaturated and subsequently grow as more vapor condenses on their surface. Aerosol dynamics is solved with the Quadrature Method of Moments [R. McGraw, *Aerosol Sci. Technol.*, 27:255-265 (1997)]. Aerosol moments advection is solved with a Lagrangian particles scheme. The results show that the highest nucleation rate region is located on the lean vapor (cool) side across the mixing layer, while particles experience a high growth rate on the rich vapor (hot) side. The effects of turbulence on particle dynamics are assessed by comparing the exact mean nucleation and growth rates with the rates evaluated from mean quantities (temperature and concentration). The nucleation rate evaluated from mean quantities tends to greatly over-estimate the mean particle number density. The growth rate evaluated from mean quantities is also higher than the exact mean value, but by a relatively small margin.

Keywords: Aerosol, Quadrature Method of Moments, Direct Numerical Simulation, Lagrangian Particles Scheme

1 Introduction

Generally, the term “aerosol” refers to a colloid suspension of fine solid particles or liquid droplets¹ in a gas. Aerosols are ubiquitous both in nature and in industrial products, for example, clouds, air pollution such as smog and smoke, soot in flames, cement dust etc. Aerosol dynamics involves various processes: nucleation, condensation, and coagulation. Aerosol particles evolution is extremely sensitive to the history of temperature and vapor concentration that these particles undergo. Therefore it is very difficult to investigate the complex interaction between turbulence mixing and aerosol growth processes. Lesniewski and Friedlander [1] measured dibutyl phthalate (DBP) particle nucleation and growth in a free turbulent jet. Garmory and Mastorakos [2] simulated aerosol evolution in the same turbulent jet using the stochastic fields method for aerosol dynamics with the Reynold’s stress turbulence model, and compared the simulation results with the experimental data of Lesniewski and Friedlander [1]. They found that considering turbulent fluctuations of temperature and concentration led to a nucleation region that was wider but with a reduced peak nucleation rate. Das and Garrick [3] simulated the formation and growth of titanium dioxide nanoparticles in incompressible planar jets by combining direct numerical simulation (DNS) for the flow field and a nodal approach for aerosol dynamics.

Aerosol particles can be described by the particle size density function (PSD), which satisfies the general dynamic equation (GDE) [4]. The GDE is a generalized convection-diffusion equation with aerosol dynamic processes serving as source terms. Analytical solutions to the GDE are available only for a few specific cases [5, 6]. The most widely employed general method and its variants for solving the GDE are based on dividing the particle size domain into sections as developed by Gelbard et al. [7]. Another method to solve the aerosol PSD evolution problem is the Monte Carlo simulation, which mimics the evolution of aerosol particles through a stochastic particle system [8–11].

¹Droplets and particles are treated as synonyms in this article.

Other than solving the PSD evolution equation, method of moments solves only a set of moments. The moments set (usually several low order moments) represents the most important fundamental information about the PSD, such as total number density, average diameter, volume fraction etc. Solving the moments set is far more economical than solving the GDE. However, owing to the nonlinearity of the aerosol dynamics, the moments dynamic equations group has of a cascade structure, i.e., higher order moments are involved in lower order moments dynamic equations. The system of equations governing a finite cut-off moments set is not closed. Many closure methods have been developed. The quadrature method of moments (QMOM) [12, 13] or its variants [14] are found to be the most accurate in general. However, QMOM requires the moment set to be realizable. A set of moments is realizable if there exists a PSD which satisfies the moment definition. Mathematically, the set of moments must satisfy the Stieltjes conditions to be realizable [15]. In numerical simulations, it is widely observed [16] that conventional advection schemes can frequently render the set of moments unrealizable.

In this work, DNS combined with QMOM is used to simulate DBP aerosol evolution in a turbulence mixing layer. To cure the moments realizability problem presented in conventional advection schemes, a Lagrangian particles scheme [17] is used to convect the moments set. The layout of this paper is as follows. In section 2, the numerical simulation settings, Lagrangian particles scheme, physical models for aerosol dynamics and QMOM are introduced. Simulation results on flow field and aerosol particles are discussed in section 3. Finally we present our conclusions.

2 Models and equations

2.1 Fluid dynamics

The direct numerical simulation presented in this work is performed by solving the unsteady, incompressible Navier-Stokes equations. The parallel flow solver “NGA” [18] developed at Stanford University is used to solve the transport equations. The solver implements a finite difference method on a spatially and temporally staggered grid with the semi-implicit fractional step method of Kim and Moin [19]. Velocity is discretized with a second order finite differences centered scheme. The time step size is calculated in order to produce a Courant-Friedrichs-Lewy number of unity. A pressure-correction step involving the solution of a Poisson equation ensures mass conservation. The code decomposes the computational domain over a number of processors and implements a distributed memory parallelization strategy using the message passing interface. The solution of the Poisson equation on massively parallel machines is performed by the library HYPRE [20] using the preconditioned conjugate gradient iterative solver coupled with one iteration of an algebraic multigrid preconditioner.

At the inlet, velocity is imposed by combining two laminar boundary layers, which have a total thickness $H = 0.011$ m. The free convective outflow [21] condition is used at the outlet. The boundary conditions are periodic in the spanwise direction z and free slip in the crosswise direction y . The free slip condition is applied by imposing a zero crosswise velocity component at the boundary. The normal derivatives of the streamwise and spanwise velocity components are set to zero. Consequently, the two velocity components parallel to the wall are free to float.

The two streams have velocity u_1 and u_2 , with $\Delta U = u_1 - u_2 = 1.0$ m/s, and $U_c = (u_1 + u_2)/2 = 1.0$ m/s. White noise with amplitude 0.4 of the velocity is superimposed on the velocity profile, resulting in the onset of Kelvin-Helmholtz instability in a very short distance downstream of the inlet. The crosswise and spanwise velocity components undergo the same type of disturbance.

The computational domain is $118H \times 94H \times 39H$, in units of the boundary layer thickness H . The size of the domain in the crosswise direction is large enough to avoid the turbulent flow field being affected by the free slip boundary conditions in any significant manner. The domain is discretized with 80 million grid points ($768 \times 398 \times 256$). The dimensions of the grid cells are the same along the three axes with $\Delta x = \Delta y = \Delta z = 0.15H$ in the region centered around $y = 0$ ($|y| \leq 22.5H$), then the grid is linearly stretched along y with a ratio 1.05 and then kept constant again, with an aspect ratio $\Delta y/\Delta x = 4$. A posteriori analysis shows $\Delta x = \Delta y = \Delta z < 3\eta$ over the whole domain, where $\eta = \nu^{3/4}\epsilon^{-1/4}$ is the Kolmogorov scale, and ν and ϵ are the kinematic viscosity and the turbulent kinetic energy dissipation rate, respectively.

Two passive scalars (temperature T and vapor mass fraction C) are simulated by solving the convection-diffusion equation using the third order WENO scheme [22]. The effect of aerosol dynamics on the temperature field is negligible (e.g., latent heat of condensation), since the vapor mass fraction is very low (maximum 5000 ppm here). For vapor

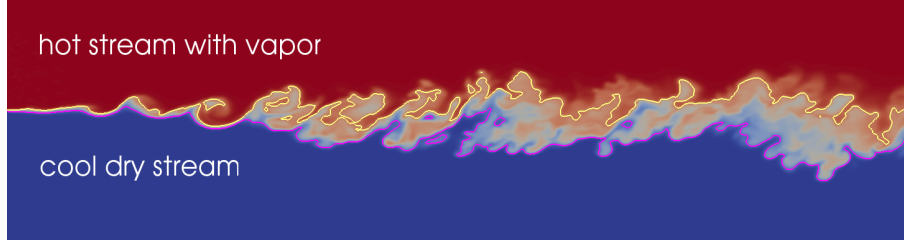


Figure 1: Snapshot of the isocontour of a scalar field in the turbulence mixing layer (clipped in y direction). The pink isocontour corresponds to the highest nucleation rate of aerosol particles, and the yellow isocontour corresponds to the fastest particle growth rate due to condensation (in the free molecule regime).

concentration, the consumption owing to aerosol dynamics is taken into account, i.e.,

$$\frac{\partial C}{\partial t} + \nabla \cdot (\vec{u}C) = D\nabla^2 C + S_{\text{Aerosol}}, \quad (1)$$

where \vec{u} is the gas flow velocity, D is the diffusivity coefficient, and the source term S_{Aerosol} denotes the vapor consumption due to gas-to-particle conversion. In the simulation, the Lewis number is assumed to be one, i.e., thermal diffusivity and mass diffusivity have the same value. The Schmidt number (ratio between kinematic viscosity and mass diffusivity) is also set to one. At the inlet, $T = 400$ K and $C = 5000$ ppm are set for the fast stream, and $T = 300$ K and $C = 0$ ppm for the slow stream. For convenience, the mixture fraction ϕ is also defined, which is a scalar in the range from 0 to 1 and is linearly proportional to T , and also to C when $S_{\text{Aerosol}} = 0$.

The simulation was performed on an IBM Blue Gene/P supercomputer, “Shaheen”, available at King Abdullah University of Science and Technology, using more than a half million CPU hours. The total simulation time is 7.1τ , where τ corresponds to the time during which the low-speed steam passes the whole domain. All mean statistics in this paper are obtained by averaging over different time instants (after a statistically steady state is reached) and the periodic z direction, with around 10 thousand samples. Figure 1 shows a snapshot of the simulated temperature field, which provides a schematic view of the simulation.

2.2 Aerosol dynamics

2.2.1 Physical models

Aerosol particles are generally described by the particle size distribution function (PSD) $n(\vec{x}, t; \xi)$, where \vec{x} denotes spatial coordinates and t is the temporal coordinate (usually termed external variables), and ξ is a parameter to describe particle morphology (internal variable). Generally, ξ can also be a vector. Here, all aerosol particles are assumed to be spherical, therefore one parameter ξ is enough to describe the particle morphology. The PSD satisfies the GDE [4]

$$\frac{\partial n}{\partial t} + \nabla \cdot n\vec{u} = \nabla \cdot D_p \nabla n + \left[\frac{\partial n}{\partial t} \right]_{\text{nucl}} + \left[\frac{\partial n}{\partial t} \right]_{\text{growth}} + \left[\frac{\partial n}{\partial t} \right]_{\text{coag}}, \quad (2)$$

where D_p is the diffusion coefficient for aerosol particles, and the last three terms on the right hand denote the aerosol dynamics. The diffusion term is usually negligible owing to the large Schmidt number for aerosol particles². Nucleation is the process by which dozens or hundreds of molecules form a stable critical nucleus particle. It is modeled by the self-consistent correction (SCC) theory [23]

$$\left[\frac{\partial n(d_p^*)}{\partial t} \right]_{\text{nucl}} = \frac{\exp[s\sigma/(k_B T)]}{S} \left[\frac{P_v x_v}{k_B T} \sqrt{\frac{2\sigma}{\pi m}} \exp\left(-\frac{16\pi\sigma^3 m^2}{3(k_B T)^3 \rho_p^2 (\ln S)^2}\right) \right]. \quad (3)$$

The SCC theory differs from the classic Becker-Döring theory [4, 24] only by the additional correction factor $\text{SCC} = \exp[s\sigma/(k_B T)]/S$. Various experimental measurements reveal that the classic nucleation theory consistently under-

²Under standard atmospheric conditions, spherical particles with a diameter of 10 nm (resp. 100 nm) have a Schmidt number equal to 290 (resp. 2.2×10^4) [4, p. 34].

estimates the nucleation rate for DBP [25, 26], even by a maximum of six orders of magnitude [27]. The SCC theory provides satisfactory prediction compared to the measurement data [27] within the temperature range of interest (300 to 400 K) for the present simulation. The magnitude of the SCC factor is of order 10^3 for the present case. In the above equation, s is the surface area of a DBP molecule, P_v is the vapor pressure, x_v is the mole fraction of the vapor, m is the molecular mass, ρ_p is the particle density, and $S = P_v/P_{\text{sat}}$ is the vapor saturation ratio. The saturation pressure P_{sat} is usually approximated by integrating the Clausius-Clapeyron equation to yield an exponential function of temperature, with two specific constants for a vapor species [28]. k_B denotes the Boltzmann constant, and σ is the surface tension. DBP is used as the nucleation and condensation material. Empirical formulas for ρ_p , P_{sat} , and σ are taken from Okuyama et al. [25]. Nucleation only generates particles with the critical diameter d_p^* , which is [4, Eqn. (9.56)]

$$d_p^* = \frac{4\sigma v_m}{k_B T \ln S}, \quad (4)$$

where v_m is the DBP molecular volume.

The particles volume growth rate due to condensation in the free molecule regime ($\text{Kn} \gg 1$, where Kn is the Knudsen number, the ratio between the mean free path of the gas and the radius of aerosol particles) is proportional to the surface area of the particles, and it is proportional to the diameter in the continuum regime ($\text{Kn} \ll 1$) [4]:

$$\left[\frac{\partial n(\xi)}{\partial t} \right]_{\text{cond}} = \frac{(p_1 - p_d) \pi \xi^2 v_m}{(2\pi m k_B T)^{1/2}}, \quad (\text{Kn} \gg 1), \quad (5)$$

and

$$\left[\frac{\partial n(\xi)}{\partial t} \right]_{\text{cond}} = \frac{2\pi \xi D (p_1 - p_d) v_m}{k_B T}, \quad (\text{Kn} \ll 1). \quad (6)$$

In the transition regime ($0.1 < \text{Kn} < 10$), the harmonic mean of the above two is used owing to its simplicity. This harmonic mean produces very similar results to the much more involved generalized Mason's formula [29].

Coagulation is the process of two particles coalescing to form a bigger particle. The coagulation dynamics is described by the Smoluchowski equation [4]

$$\left[\frac{\partial n(\xi)}{\partial t} \right]_{\text{coag}} = \frac{1}{2} \int_0^\xi \beta n(\tilde{\xi}) n(\xi - \tilde{\xi}) d\tilde{\xi} - \int_0^\infty \beta n(\xi) n(\tilde{\xi}) d\tilde{\xi}. \quad (7)$$

The collision kernel function $\beta(\xi, \tilde{\xi})$ describes the rate at which particles of size ξ coagulate with particles of size $\tilde{\xi}$. In the free molecule and continuum regimes, β is obtained from well established theories [4]:

$$\beta(\xi, \tilde{\xi}) = \left(\frac{6}{\pi} \right)^{2/3} \left(\frac{\pi k_B T}{2\rho_p} \right)^{1/2} \left(\frac{1}{\xi} + \frac{1}{\tilde{\xi}} \right)^{1/2} (\xi^{1/3} + \tilde{\xi}^{1/3})^2, \quad (\text{Kn} \gg 1), \quad (8)$$

and

$$\beta(\xi, \tilde{\xi}) = \frac{2k_B T}{3\mu} \left(\frac{1}{\xi^{1/3}} + \frac{1}{\tilde{\xi}^{1/3}} \right)^{1/2} (\xi^{1/3} + \tilde{\xi}^{1/3}), \quad (\text{Kn} \ll 1), \quad (9)$$

where μ is the gas viscosity. As in the treatment of condensation, the harmonic mean is used in the transition regime.

2.2.2 Quadrature method of moments (QMOM)

Other than directly solving the PSD from the GDE Eqn. (2), only a few moments are solved in the QMOM. The k th ($k = 0, 1, 2, \dots$) order moment is defined as

$$M_k = \int_0^\infty n L_p^k dL_p, \quad (10)$$

where L_p denotes the particle size, which can be diameter or volume. Here, diameter is used. Accordingly, M_0 means the particle number density ($\#/m^3$), M_1 the diameter "density" (m/m^3), $4\pi M_2$ the surface area "density" (m^2/m^3), and $\pi M_3/6$ the volume fraction (m^3/m^3), etc. Four moments (from M_0 to M_3) are tracked in this simulation. The dynamic equations for the moments set are obtained by applying the moment transformation to the GDE, i.e.,

multiplying by L_p^k and integrating over the particle size space to render (The convection term is not included, which is dealt with by the Lagrangian particles scheme discussed in the next section.)

$$\frac{\partial M_k}{\partial t} = S_{\text{nucl}}(M_i) + S_{\text{cond}}(M_i) + S_{\text{coag}}(M_i), \quad (i \in 0, 1, \dots, k, \dots) \quad (11)$$

Owing to the nonlinearity in the GDE, the moments equations are not closed. High order moments appear in the equations for low order moments. QMOM [12] is used to close the equations. The basic idea of QMOM is to use N point Gaussian quadrature to approximate the integration in transforming the GDE to moments equations, i.e., the PSD is assumed to be [14]

$$n = \sum_{i=1}^N W_i \delta(L - L_i), \quad (12)$$

where $\delta()$ is the Dirac delta function, L_i is the abscissa (diameter here), W_i is the corresponding weight, and N denotes how many delta functions are used to approximate the PSD (here $N = 2$). Then all the source terms on the right hand side of Eqn. (11) can also be expressed in terms of L_i and W_i ([14]). However, L_i and W_i are not determined yet, they are required to satisfy

$$M_k = \int_0^\infty n L_p^k dL_p = \sum_{i=1}^N L_i^k W_i. \quad (13)$$

Grouping Eqns. (11) and (13) for $k = 0, 1, \dots, 2N - 1$, there are $4N$ equations and $4N$ unknowns ($2N$ for M_k , N for W_i and L_i); these differential algebraic equations are then closed. From a set of $2N$ initial moments $M_k(0)$, the so-called product difference scheme [12] can be used to find the N abscissas and weights according to Eqn. (13). The abscissas and weights are then substituted into the moments dynamic Eqns. (11) to integrate for one time step. The ODE solver DOPRI5 [30] is used to integrate the equations.

To apply the product difference scheme, the moments set must be realizable. A set of moments is realizable if there exists a PSD which satisfies the moment definition Eqn. (10). Mathematically, the set of moments must satisfy the Stieltjes conditions to be realizable [15]. Returning to the aerosol evolution problem, a moment cannot evolve independently, and the whole moments set should evolve as a “vector” subject to certain constraints [16]. The Lagrangian particles scheme used here transports the moments “vector” as a whole, which successfully avoids the moments realizability problem usually encountered in conventional advection schemes [16].

2.3 Lagrangian particles scheme

The previous section discusses how the aerosol particles evolution is treated by the QMOM. Here, the Lagrangian particles³ scheme [17, 31] used to solve the advection of the moments set M_k is introduced.

Generally, in particle methods, functions and differential operators are replaced by equivalent integral representations, discretized using particles [32]. Particles are mathematical objects representing one or more physical properties, such as temperature, mixture concentration, vorticity, statistical moments of aerosols, etc. The physical properties are evolved by solving a set of ordinary differential equations for the particles’ trajectories (\vec{x}^p) and property values ($\vec{\omega}^p$):

$$\frac{d\vec{x}^p}{dt} = \vec{u}^p = \sum_N G(\vec{x}^p, \vec{\omega}^p, t, \dots) \quad p = 1, \dots, N \quad (14)$$

$$\frac{d\vec{\omega}^p}{dt} = \sum_N F(\vec{x}^p, \vec{\omega}^p, t, \dots) \quad p = 1, \dots, N \quad (15)$$

where \vec{x}^p and \vec{u}^p denote the location and the velocity of particle p , $\vec{\omega}^p$ represents the property vector, and G and F describe the system dynamics. The underlying function represented by the particles at discrete, and not regularly spaced, points can be approximated as a generalized function (smooth in the sense of the measure) using a sum of

³Except where explicitly stated, particles in this subsection refer to mathematical objects, rather than physical aerosol particles as discussed elsewhere in this paper.

delta distributions:

$$\vec{\omega}(\vec{x}, t) = \sum_{p=1}^N \vec{\omega}^p(t) \delta(\vec{x} - \vec{x}^p(t)). \quad (16)$$

Although the distribution in Eqn. (16) is well defined, it is desirable to obtain a regular representation (i.e. a differentiable function) of the underlying Eulerian field. Such a representation is obtained via regularization by convolution with a *mollification* kernel ζ_l of width l :

$$\vec{\omega}(\vec{x}, t) \sim (\vec{\omega} \star \zeta_l)(\vec{x}, t) = \sum_{p=1}^N \vec{\omega}^p(t) \zeta_l(\vec{x} - \vec{x}^p(t)). \quad (17)$$

Specifically, the advection of aerosol moments is solved with the Lagrangian particle approach:

$$\frac{d\vec{x}^p}{dt} = \vec{u}(\vec{x}^p) \quad \text{and} \quad \frac{dM_k^p}{dt} = S^p, \quad (18)$$

where $\vec{u}(\vec{x}^p)$ is the Eulerian velocity evaluated at the particle position \vec{x}^p , M_k^p represents the aerosol moments associated with particle p , and S_k^p is the source term, which is evaluated according to Eqn. (11) for each particle p . Since the gas phase velocity \vec{u} is known from solving the Navier-Stokes equations at every grid point, $\vec{u}(\vec{x}^p)$ is obtained by interpolating on \vec{u} with a tri-linear interpolation scheme.

If required, the solution obtained with the particle method can be projected via the mollification kernel on a grid that may or may not coincide with that used for the velocity and scalar fields. The projection of the Lagrangian solution on the Eulerian grid is needed to post process the data and to compute source terms for the Eulerian scalars, thus enabling a two way coupling between the aerosol and the gas phase. A box average is used as a regularization kernel:

$$M_k(\vec{x}) = \frac{1}{N_\Omega} \sum_{p \in \Omega} M_k^p, \quad (19)$$

where Ω is the set of particles located inside a cell of size l and N_Ω the number of such particles.

The accuracy, resolution, and costs of the Lagrangian solver depend strongly on the number of particles used for the simulation. Due to the interaction between numerical errors in the particles' positions and the topology of the advecting velocity field, the particle density is not spatially homogeneous and regions with a small number of particles develop. If a grid cell does not contain any particles, the Eulerian field $M_k(\vec{x}, t)$ and two-way coupling source terms cannot be computed.

The adverse effects associated with regions of low Lagrangian particle density can be mitigated in different ways: (i) increasing the total number of particles in the domain, (ii) using a mollification kernel with a larger width, or (iii) reinitializing the particle field onto a regularized set of particles (remeshing) [32, 33]. Given that the cost of the Lagrangian method scales linearly with the number of particles, increasing the number of particles may result in prohibitive computational expense. For aerosol simulations, the overhead can be significant because the source terms are computationally expensive compared to all other costs (i.e. velocity and scalar transport). Conversely, varying the kernel width has a negligible effect on computational costs, but increases the numerical diffusion in the reconstructed Eulerian field $M_k(\vec{x}, t)$. Particle reinitialization is usually the preferred approach [33, 34], but it is not used in the present work so as to preserve the realizability of the moment set [16]. A combination of methods (i) and (ii) is used in this simulation.

3 Results and discussion

3.1 Velocity field

It is well known that at a certain distance from the inlet, the mixing layer evolves self similarly. The momentum thickness δ_θ is used to measure the local layer thickness, which is defined as

$$\delta_\theta(x) = \frac{1}{\Delta U^2} \int_{-\infty}^{\infty} (u_1 - \bar{u})(\bar{u} - u_2) dy, \quad (20)$$

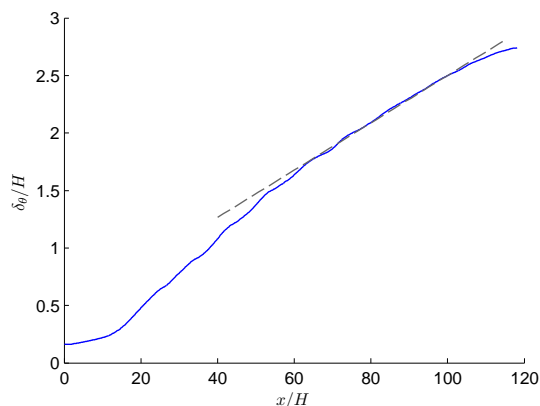


Figure 2: Streamwise evolution of the normalized momentum thickness δ_θ/H . The dashed line is obtained with a least square fit in the range $60 < x/H < 100$; the slope of the line is 0.0206.

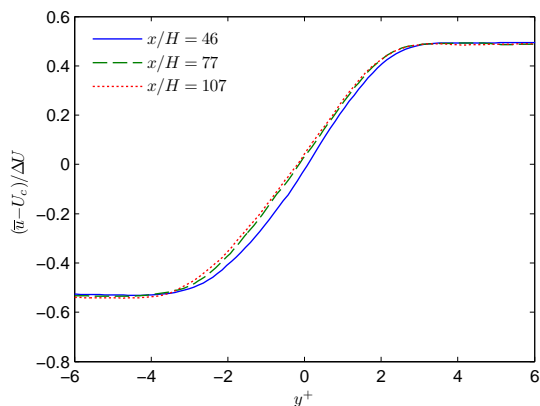


Figure 3: Mean streamwise velocity profiles at several downstream locations.

where the bar symbol denotes statistical mean. The nondimensionalized crosswise coordinate is defined as $y^+(x) = y/\delta_\theta(x)$. Self similarity implies a linear growth for the total turbulent kinetic energy $K(x)$ [35], which is defined as

$$K(x) = \int_{-\infty}^{\infty} k \, dy = \frac{1}{2} \int_{-\infty}^{\infty} \overline{u'u'} + \overline{v'v'} + \overline{w'w'} \, dy, \quad (21)$$

where, k is the turbulent kinetic energy, u' , v' and w' are the components of the fluctuation velocity.

Figure 2 shows the streamwise evolution of the normalized momentum thickness δ_θ/H . From $x/H = 60$ downwards, linear growth is observed, except for slight deviation near the outlet, which may be related to the cross domain size or the outlet boundary condition. The slope of the fitted line is 0.0168 in the simulation [35], but a slightly higher value 0.0206 is obtained here, which still lies in the measured range between 0.014 and 0.022 [36]. Figure 3 shows the mean streamwise velocity profiles at several downstream locations. Profiles at $x/H = 77$ and $x/H = 107$ are nearly identical, another sign of self similarity. The streamwise evolution of the total turbulent kinetic energy is shown in Fig. 4. Linear growth is observed for $x/H > 60$. It is also found that $K_x > K_z > K_y$ in the self similarity region, which also agrees with the findings in the simulation [35].

3.2 Passive scalar

Similar to the velocity field, the mean profile of a passive scalar exhibits self similarity from a certain distance away from the inlet. Figure 5 shows the mean mixture fraction profiles at several downstream locations. The profiles at $x/H = 77$ and 107 are almost identical.

Figure 6 shows the mean total streamwise flux of vapor concentration. Coupled and uncoupled cases are compared.

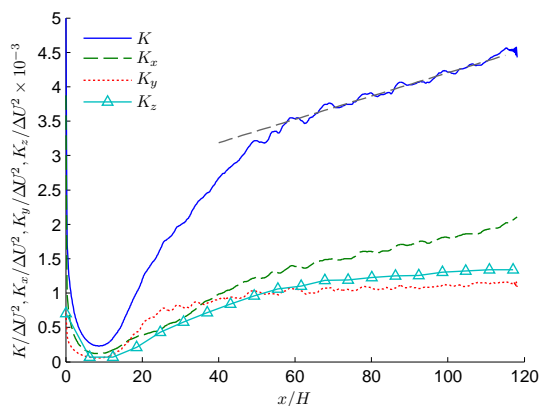


Figure 4: Streamwise evolution of normalized total turbulent kinetic energy K . K_x , K_y and K_z are components in three directions. The dashed line is obtained with a least square fit of K in the range $60 < x/H < 100$.

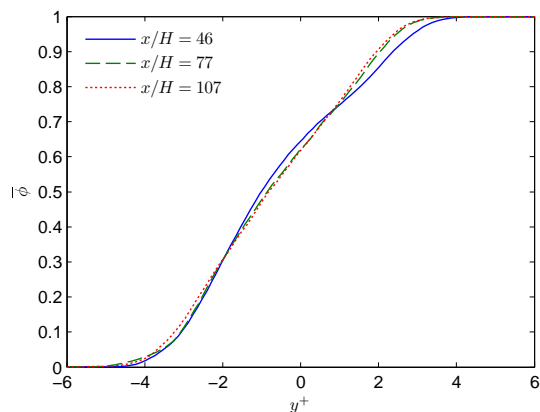


Figure 5: Mean mixture fraction profiles at several downstream locations.

In the coupled case the vapor consumption due to gas-to-particle conversion has been taken into account. As expected, the mean flux is constant (except for statistical fluctuation) along the streamwise direction for the uncoupled case, and decreases for the coupled case. Conservation property of the vapor can be used to check the correctness of the coupling between vapor transport and aerosol evolution. The consumed vapor due to gas-to-particle conversion can be evaluated as $\pi M_3/6 \times m_{\text{DBP}}/m_{\text{gas}}$, where $\pi M_3/6$ is the volume fraction of aerosol particles, $m_{\text{DBP}}/m_{\text{gas}}$ is the ratio of DBP and the carrier gas molecular weights. Taking the vapor consumption into account, the total vapor flux is conserved (curve “coupled+aerosol consumption”).

The probability density function (pdf) of the mixture fraction (representative for T and C) is vital for the determination of mean nucleation and condensation rates. Figure 7 shows the pdf at various positions along the streamwise and crosswise directions. The crosswise positions are chosen according to the mean value of ϕ . Qualitatively the same behaviors with those found by Attili and Bisetti [35] are observed. They discussed the marching and non-marching behaviors of the peak of a pdf. A marching pdf always has its peak at its mean value position across the layer, while a non-marching pdf does not have this property. Thus, in the transition region ($x/H = 300$) the pdf is non-marching, since nearly all pdfs peak around $\phi = 0.7$. Gradually, the pdf becomes marching as the mixing layer evolves downstream, an indication that turbulence is well developed [35]. The pdf corresponding to $\bar{\phi} = 0.3$ has a very high tail towards $\phi = 0$, which becomes smaller as the pdf evolves along the streamwise direction. Towards $\phi = 1$, the tail of the pdf is much smaller compared to that towards $\phi = 0$. In the present simulation, $\phi = 1$ means the scalar is carried by the fast stream. This different behavior of the pdf tail may be related to the difference in turbulence intermittency in the fast and slow stream sides.

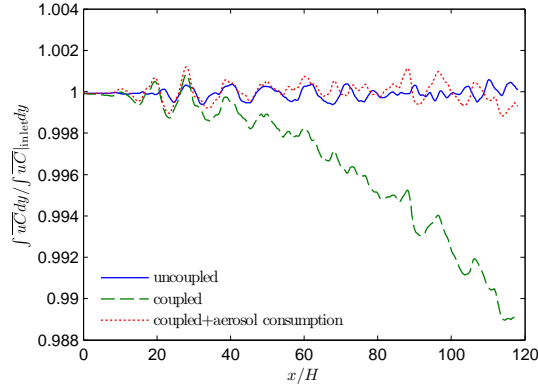


Figure 6: Streamwise evolution of the integrated mean vapor flux along the crosswise direction. $\overline{uC}|_{inlet}$ denotes mean flux at the inlet. In the coupled solution, the consumption from aerosol dynamics has been taken into account; in the uncoupled solution, the source term in Eqn. (1) is set to zero. Aerosol consumption is evaluated as $\pi M_3/6 \times m_{DBP}/m_{gas}$, where $\pi M_3/6$ is the volume fraction of aerosol particles, and m_{DBP}/m_{gas} is the ratio of the molecular weights of DBP and the carrier gas .

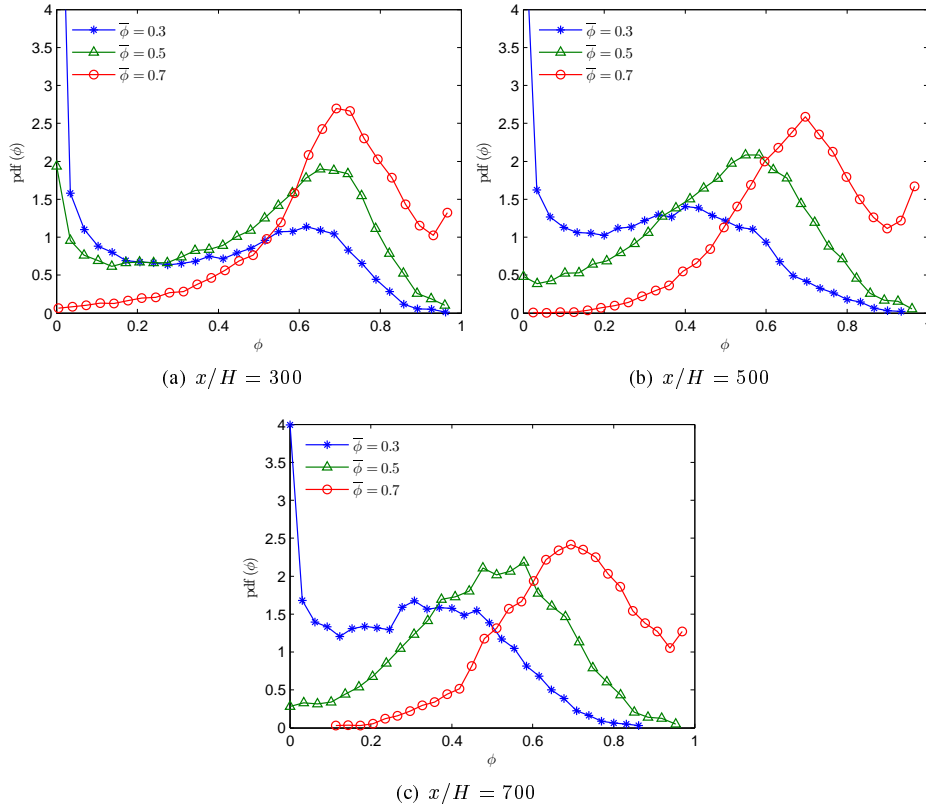


Figure 7: Probability density function of the mixture fraction ϕ at various positions, with streamwise positions $x/H = 300, 500,$ and $700,$ and crosswise positions corresponding to mean ϕ value of $0.3, 0.5,$ and $0.7.$

3.3 Aerosol dynamics

An important practical question is whether it is acceptable to estimate the mean aerosol production and growth rate from the mean quantities (\bar{T} and \bar{C}) in turbulence, since the pdfs of T and C are usually too expensive to obtain, while \bar{T} and \bar{C} can be estimated much more easily. It has been found [2, 37–39] that calculating nucleation, growth and coagulation terms as functions of mean quantities can lead to significant errors compared to correctly including the effect of turbulence-induced fluctuation. Using DNS, it is possible to quantify the effect of turbulent fluctuations of temperature and concentration on the mean nucleation and growth rate of aerosol.

For the nucleation rate, it is desirable to compare $\overline{I_{\text{nuc}}(T, C)}$ with $I_{\text{nuc}}(\bar{T}, \bar{C})$, i.e., the exact mean nucleation rate and the rate evaluated from the mean of T and C . If the vapor consumption due to gas-to-particle conversion is neglected, the T and C fields are linearly correlated, and both can be reconstructed from the mixture fraction ϕ through a simple linear transformation, i.e., $T = (T_{\text{max}} - T_{\text{min}})\phi + T_{\text{min}}$ and $C = (C_{\text{max}} - C_{\text{min}})\phi + C_{\text{min}}$, where the subscripts max and min denote the maximum and minimum values set at the inlet. Under these conditions, the nucleation rate function can be simplified to the form $I_{\text{nuc}}(\phi)$. Figure 8 shows the function $I_{\text{nuc}}(\phi)$ corresponding to present boundary conditions. The nucleation rate has a sharp peak at $T = 317\text{K}$ or equivalently $\phi = 0.17$, then decreases to zero very quickly away from the peak. Figure 8 provides strong clues to understanding the nucleation process in the flow.

Figure 9(a) shows the mean nucleation rate profiles at different cross sections. $I_{\text{nuc}}(\bar{T}, \bar{C})$ has an outstanding peak at the lean vapor (cool) side across the mixing layer. The curve shape is very similar to that in Fig. 8. $\overline{I_{\text{nuc}}(T, C)}$ is far more flat, and covers a broader region. The peak of $\overline{I_{\text{nuc}}(T, C)}$ can be one order of magnitude smaller than that of $I_{\text{nuc}}(\bar{T}, \bar{C})$. This phenomenon can be explained by investigating the pdf (Fig. 7) and the nucleation rate function (Fig. 8). Recall that [40]

$$\overline{I_{\text{nuc}}(T, C)} = \iint I_{\text{nuc}}(T, C) \text{pdf}(T, C) dT dC \approx \int I_{\text{nuc}}(\phi) \text{pdf}(\phi) d\phi, \quad (22)$$

and $I_{\text{nuc}}(\phi)$ is similar to a Dirac Delta function. The broad distribution of the pdf makes it impossible to miss the region where $I_{\text{nuc}}(\phi)$ is extremely high, hence $\overline{I_{\text{nuc}}(T, C)}$ extends broadly across the mixing layer. On the other hand, $\overline{I_{\text{nuc}}(T, C)}$ cannot reach the maximum of $I_{\text{nuc}}(T, C)$, since $\text{pdf}(T, C)$ is generally not concentrated in the maximum nucleation rate region. However, the case is very different for $I_{\text{nuc}}(\bar{T}, \bar{C})$. Actually, it has been derived that $I_{\text{nuc}}(\bar{T}, \bar{C}) \approx I_{\text{nuc}}(\phi)$. The finding that $\overline{I_{\text{nuc}}(T, C)}$ has a wider nucleation region but with a reduced peak nucleation rate compared with $I_{\text{nuc}}(\bar{T}, \bar{C})$, agrees with the analysis [37] and the numerical simulation [2]. In addition, the peak of $\overline{I_{\text{nuc}}(T, C)}$ is found to shift towards the center of the mixing layer, compared with $I_{\text{nuc}}(\bar{T}, \bar{C})$.

Figure 9(b) shows streamwise evolution of the integrated nucleation rate along the cross direction, which determines the streamwise evolution of the total number density (i.e., crosswise integrated number density). It is found that the value corresponding to $I_{\text{nuc}}(\bar{T}, \bar{C})$ is systematically higher than that corresponding to $\overline{I_{\text{nuc}}(T, C)}$, except in the region very close to the inlet. This suggests that to evaluate number density from $I_{\text{nuc}}(\bar{T}, \bar{C})$ would result in systematic overestimation. In this simulation, the vapor concentration is coupled with the consumption from nucleation and condensation processes. The total nucleation rate in the uncoupled case continues to increase almost linearly along the streamwise direction. However, the rate in the coupled case first increases owing to enhanced turbulence mixing, then decreases because of decreasing vapor concentration due to gas-to-particle conversion. The difference in the rates between the uncoupled and coupled cases increases along the streamwise direction. Near the outlet, the total nucleation rate in the uncoupled case is one order higher than that in the coupled case, although the vapor concentration in the coupled case is at most 10% lower than that in the uncoupled case throughout the whole flow field. To better understand how nucleation is affected by vapor consumption, Fig. 10 shows the mean vapor consumption in the mixture fraction space. The maximum consumption rate appears at $\phi = 0.65$ for $x/H = 15$, and then the peak rate shifts to $\phi = 0.55$ for $x/H = 107$. Nucleation mostly happens around the region $\phi = 0.17$, but it consumes a negligible amount of vapor, because the nucleated particles are so small (a few nanometers). Vapor is consumed mainly due to condensation.

Similar to the analysis for nucleation, the particles growth rate due to condensation can also be simplified to the function form $G_{\text{cond}}(\phi)$. However, except for the free molecule regime, the particle growth rate also depends on its diameter (d). Figure 11(a) shows the growth rate for particles from 1 nm to 10 micron at various temperatures (also various vapor concentrations). From 1 nm to 0.1 micron (generally in the free molecular regime), the growth rate is nearly constant. From 0.1 micron onwards the growth rate keeps decreasing as particles become bigger. Growth in the free molecule regime is of greater interest for its high rate. Since the growth rate is independent of the diameter in the

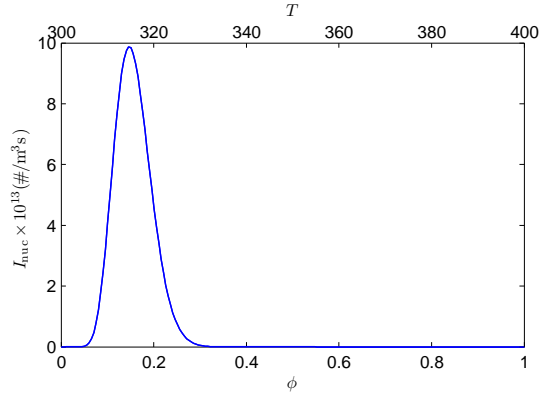


Figure 8: Nucleation rate function.

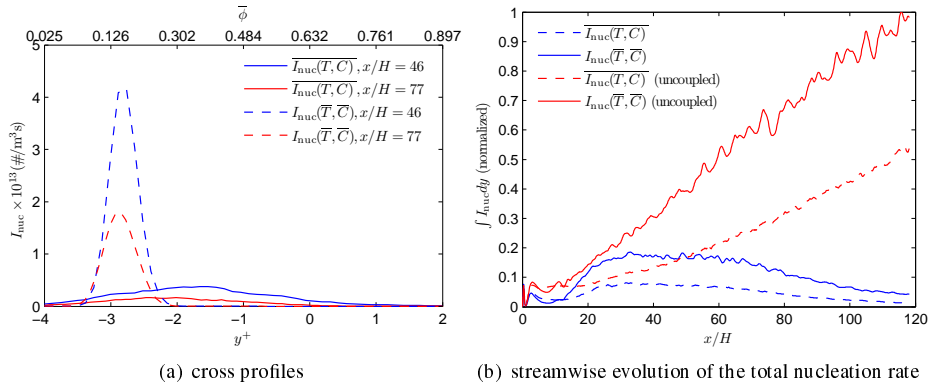


Figure 9: Nucleation rate. $\bar{\phi}$ corresponds to $x/H = 77$ in (a); Uncoupled solutions denote that vapor consumption from nucleation and condensation processes has not been taken into account in the control equation for vapor concentration.

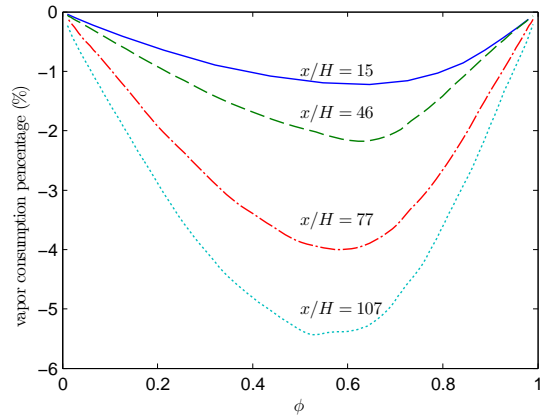


Figure 10: Vapor consumption with respect to mixture fraction.

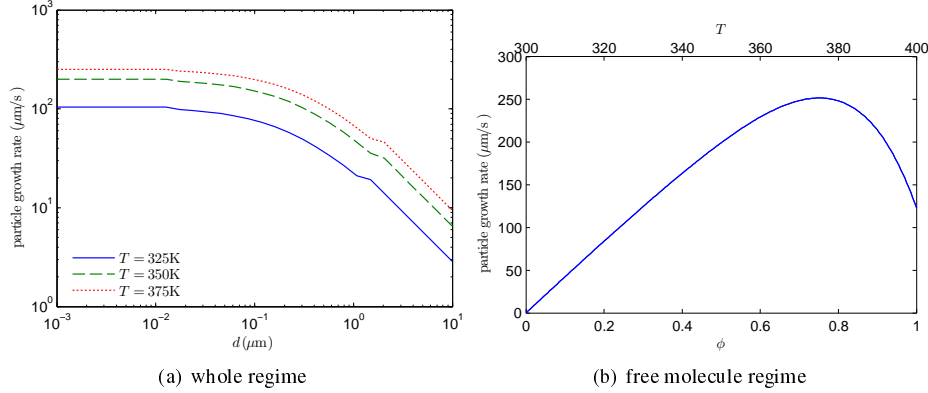


Figure 11: Functions of particle diameter growth rate due to condensation.

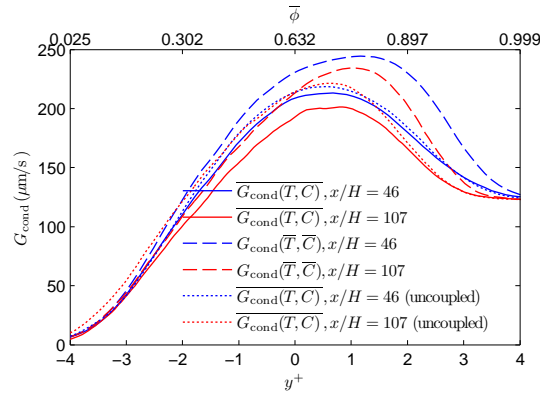


Figure 12: Particle diameter growth rate due to condensation. $\bar{\phi}$ corresponds to $x/H = 76$. Uncoupled solutions denote that aerosol consumption of vapor has not been taken into account in the vapor concentration control equation.

free molecule regime, it is possible to give the function curve [Fig 11(b)] as for nucleation. Unlike nucleation which favors low temperature, the condensation growth rate has a peak towards high temperature at $T = 375$ K. The growth rate changes mildly over the whole temperature range, in stark contrast to the spiky nucleation rate function.

Figure 12 compares the exact mean growth rate $G_{\text{cond}}(T, C)$ with $G_{\text{cond}}(\bar{T}, \bar{C})$ at various cross sections. All profiles have a similar shape, and also resemble the growth rate function in the free molecule regime [Fig. 11(b)]. $G_{\text{cond}}(\bar{T}, \bar{C})$ is found to be always higher than $G_{\text{cond}}(T, C)$, with a ratio of nearly 40% at around $y^+ = 1$ [corresponding to $\bar{T} = 375$ K, at which the growth rate obtains the maximum (Fig. 11)(b)]. The peak of $G_{\text{cond}}(T, C)$ is found to shift towards the center of the mixing layer, compared with $G_{\text{cond}}(\bar{T}, \bar{C})$. The uncoupled solution overestimates the growth rate, but only by a fractional amount at $x/H = 46$. This overestimation increases along the streamwise direction, as the accumulated consumption of vapor.

Coagulation is a very complex process, which is determined by the integro-differential Eqn. (7). It is impossible to analyze coagulation as for nucleation and condensation. Coagulation will reduce particles' number density, and increase their size. The effect of coagulation on the evolution of the total particle number density [$N_\infty = \int n(\xi) d\xi$] can be modeled as [4, p. 234]

$$\frac{dN_\infty}{dt} = -\frac{1}{2} \int_0^\infty \int_0^\infty \beta(\xi, \tilde{\xi}) n(\xi) n(\tilde{\xi}) d\tilde{\xi} d\xi. \quad (23)$$

Then, it is possible to estimate the magnitude of dN_∞/dt and compare it with the nucleation rate. $\beta(\xi, \tilde{\xi})$ obtains its maximum value when ξ is a few nanometers and $\tilde{\xi}$ is a few microns, corresponding to the smallest (ξ_{min}) and largest (ξ_{max}) particles in this simulation, respectively. It is clear that $|dN_\infty/dt|$ reaches its maximum value when the PSD

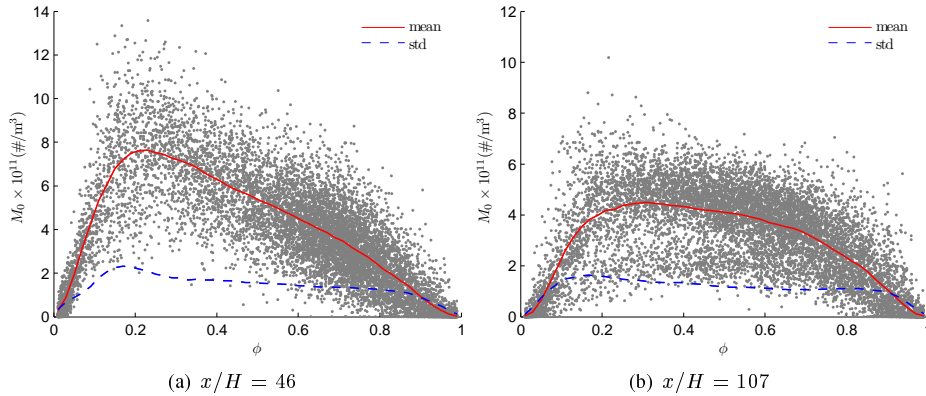


Figure 13: Scatter plots for M_0 .

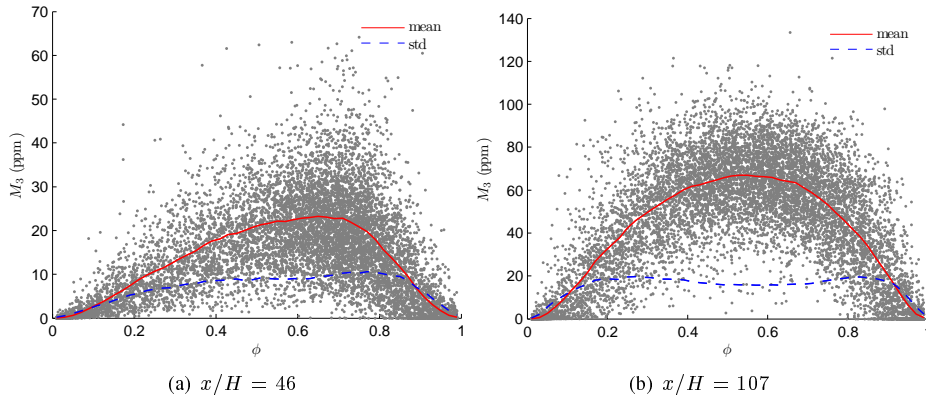


Figure 14: Scatter plots for M_3 .

has a double peaked distribution

$$n(\xi) = \begin{cases} N_\infty/2, & \xi = \xi_{\min} \text{ or } \xi_{\max}, \\ 0, & \text{otherwise,} \end{cases} \quad (24)$$

i.e., half the particles have size ξ_{\min} , the other half have size ξ_{\max} . In the simulation, the maximum value of N_∞ is around 10^{12} ($\#/m^3$). Hence, the estimated maximum rate of $|dN_\infty/dt|$ is of order 10^{13} ($\#/m^3s$), which is comparable to the maximum nucleation rate. However, the occurrence of such an extreme case is almost impossible; the real coagulation rate should be much smaller. $|dN_\infty/dt|$, estimated from a mono dispersed PSD of all particles with the average diameter (a few microns), is three orders smaller than the maximum nucleation rate. Unlike coagulation, nucleation would reach its maximum rate in a layer throughout the mixing layer (as marked in Fig. 1). Hence, it can be concluded that coagulation has a much smaller impact on determining the total particle number density than nucleation in this simulation.

To further investigate the aerosol growth processes in the mixing layer, scatter plots for M_0 , M_3 and $d = M_1/M_0$ are given in figures 13, 14, and 15. These scatter plots demonstrate how aerosol moments are correlated with the mixture fraction. Sample data at two cross sections $x/H = 300$ and $x/H = 700$ are shown. Essentially, the plots exhibit qualitatively the same trend at the two cross sections. For M_0 (Fig. 13), the mean curve has a peak towards the lean vapor side, which agrees with the analysis of Fig. 8. The peak becomes less prominent along the streamwise direction [comparing (a) and (b) in Fig. 13], because the nucleation rate decreases due to vapor consumption. For M_3 (Fig. 14), the peak of the mean curve ($x/H = 46$) appears near $\phi = 0.7$, close to the position corresponding to the maximum growth rate (Fig. 11). Along the streamwise direction, the peak shifts toward the center. For the average diameter d , the mean curve closely resembles that in Fig. 11(b), which provides a clue that the particle growth is dominated by condensation in the free molecule regime.

Figure 16 shows snapshots of instantaneous moments fields of M_0 and M_3 . M_0 is the particle number density,

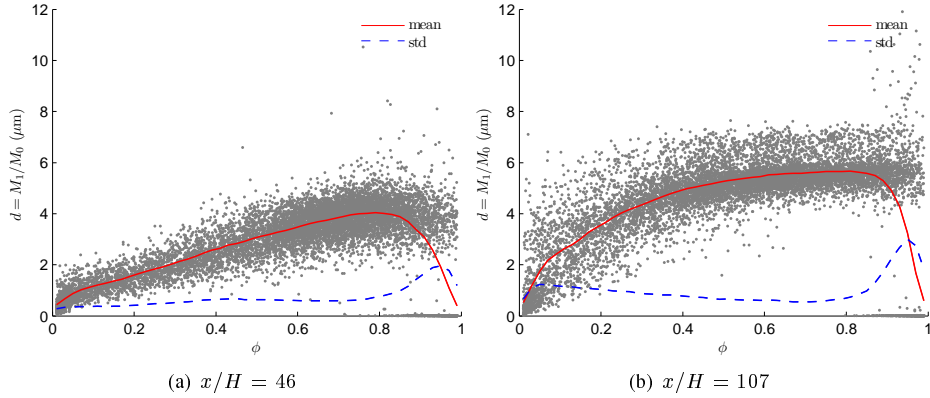


Figure 15: Scatter plots for average diameter $d = M_1/M_0$.

mainly determined by the nucleation process (coagulation is too weak to affect the number density significantly). The highest number density appears in the mixing layer towards the lean vapor side (lower side in the figure), which agrees with the analysis of the nucleation rate function. M_3 is the volume fraction (lacking a factor $\pi/6$). It increases along the streamwise direction, due to vapor condensing incessantly on existing particles.

To investigate the streamwise evolution of moments, total moments are defined similarly to the total kinetic energy as in Eqn. (21). Figure 17 shows the evolution of the total moments, which are normalized by their corresponding maximum values. Generally, all moments increase along the streamwise direction. However, a constant plateau is observed before $x/H = 20$ for all the moments. Within this region, the mixing layer is laminar. It implies aerosol processes are very slow in laminar diffusion flows. In the turbulent mixing region ($x/H > 20$), higher order moments have a faster increasing rate, because particle diameter increases along the streamwise direction, and high order moments involve high power of the diameter, and so increase faster.

Figure 18 shows the cross profiles of moments at various streamwise positions. Profiles for $\overline{M_0}$ are given in subfigure (a). All the peaks of $\overline{M_0}$ at different downstream positions appear nearly in the same location, corresponding to the peak of $\overline{I_{\text{nuc}}}(T, C)$ in Fig. 9(a). From $x/H = 77$ to 107, the peak value of M_0 decreases slightly. This is mainly due to the factor that condensation continues to consume vapor (nucleation consumes a negligible amount of vapor, because the nucleated particles are too small), which causes the nucleation rate to become smaller downstream. Subfigure (b) gives the M_1 profile. The peak value increases along the streamwise direction, but at an even slower rate. M_3 increases almost linearly along the streamwise direction. The profiles for the average diameter are also shown [subfigure (d)]. In method of moments, the average diameter is not solved directly, but derived from the known moments. It can be defined as M_1/M_0 or $(M_3/M_0)^{1/3}$. From the figure it can be seen that $(M_3/M_0)^{1/3}$ is systematically higher than M_1/M_0 , but both exhibit practically the same behavior. The diameter increases along the streamwise direction, but is nearly constant across the mixing layer. Taking into account the fact that particles start growing from around 2 nm (critical size from nucleation), we can observe that particles grow very fast due to condensation.

4 Conclusion

In this work, the nucleation and growth of dibutyl phthalate particles in a turbulent mixing layer has been simulated through the combination of direct numerical simulation for the flow field and the quadrature method of moments for aerosol dynamics. A Lagrangian particles scheme is used to transport the moments of the particle size density function. The scheme circumvents the problem of the realizability of moments, which is usually encountered in conventional advection schemes. The effects of turbulence on particle dynamics are assessed by comparing the exact mean nucleation and growth rates with the rates evaluated from mean quantities (temperature and concentration). This simulation of a developing mixing layer also shows that the turbulent fluctuations of temperature and concentration lead to a nucleation region that was wider but with a reduced peak nucleation rate (compared with the nucleation evaluated from the mean quantities), which was found in a free turbulent jet flow both by analysis [37] and numerical simulation [2]. Turbulent fluctuation is found always to inhibit particle growth for DBP particles (i.e., the exact mean

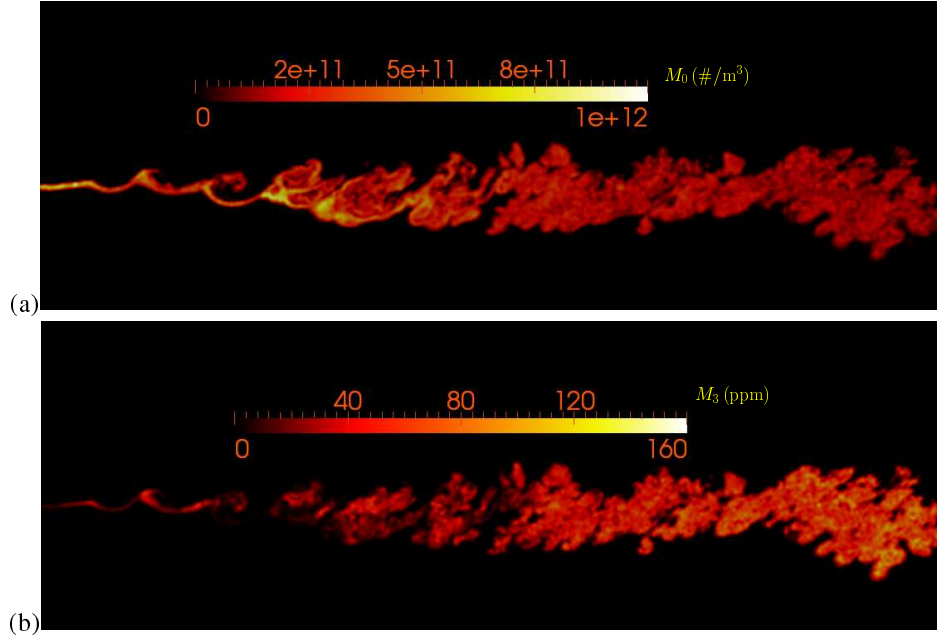


Figure 16: Snapshots of instantaneous fields. (a). M_0 ; (b). M_3 .

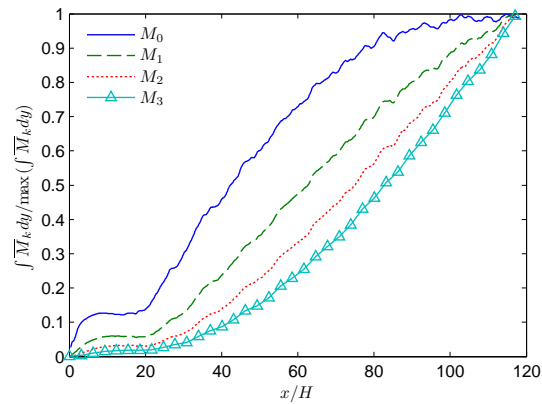


Figure 17: Streamwise evolution of the integrated mean moments along the crosswise direction, normalized by their corresponding maximum values in the whole range.

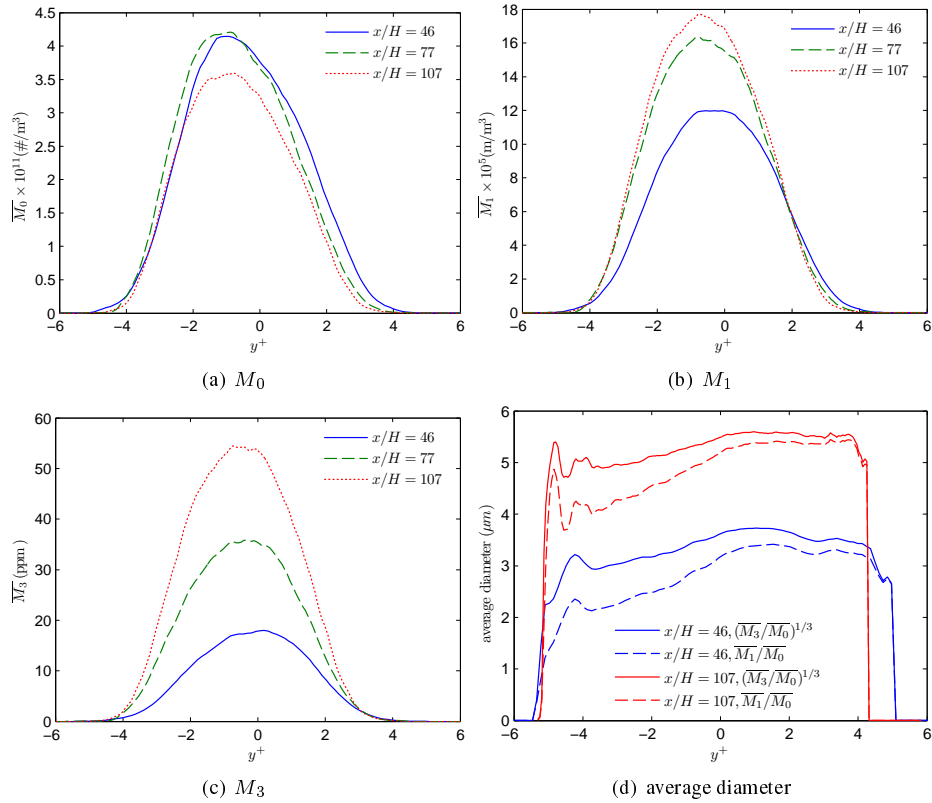


Figure 18: Cross profiles of moments and average diameter.

growth rate is always smaller than the rate evaluated from the mean temperature and concentration). However, Das and Garrick [3] found that turbulent fluctuation can both augment and inhibit titanium dioxide particle growth, although the predominant effect is to reduce particle growth. Therefore the effect of turbulent fluctuation on particle growth of various aerosols may vary, due to different shapes of the growth rate function.

Most particles are nucleated on the lean (cool) vapor side in the mixing layer. However, particles experience a high growth rate due to condensation on the rich (hot) vapor side. Owing to turbulent transport, the mean cross profiles of number density and volume fraction peak near the center of the mixing layer. The average diameter is almost constant across the layer.

Acknowledgment

Amjad Sha'arawi helped to prepare the DNS simulation; his work is thankfully acknowledged.

References

- [1] Thomas K. Lesniewski and Sheldon K. Friedlander. Particle nucleation and growth in a free turbulent jet. *Proc. R. Soc. Lond. A*, 454:2477–2504, 1998.
- [2] A. Garmory and E. Mastorakos. Aerosol nucleation and growth in a turbulent jet using the Stochastic Fields method. *Chem. Eng. Sci.*, 63(16):4079–4089, 2008. doi: 10.1016/j.ces.2008.05.012.
- [3] Shankhadeep Das and Sean C. Garrick. The effects of turbulence on nanoparticle growth in turbulent reacting jets. *Phys. Fluids*, 22:103303, 2010. doi: 10.1063/1.3486203.

- [4] S. K. Friedlander. *Smoke, Dust, and Haze: Fundamentals of Aerosol Dynamics*. Oxford University Press, New York, second edition, 2000.
- [5] T. W. Peterson, F. Gelbard, and J. H. Seinfeld. Dynamics of source-reinforced, coagulating, and condensing aerosols. *J. Colloid Interf. Sci.*, 63:426–445, 1978.
- [6] F. Gelbard and J. H. Seinfeld. The general dynamics equation for aerosols. *J. Colloid Interface Sci.*, 68(2): 363–382, 1979.
- [7] F. Gelbard, Y. Tambour, and J. H. Seinfeld. Sectional representations for simulating aerosol dynamics. *J. Colloid Interface Sci.*, 76(2):541–556, 1980.
- [8] D. Gillespie. The stochastic coalescence model for cloud droplet growth. *J. Atmos. Sci.*, 29:1496–1510, 1972. doi: 10.1175/1520-0469(1972)029<1496:TSCMFC>2.0.CO;2.
- [9] A. A. Lushnikov. Certain new aspects of the coagulation theory. *Izv. Atmos. Ocean Phys.*, 14:738–743, 1978.
- [10] A. Eibeck and W. Wagner. An efficient stochastic algorithm for studying coagulation dynamics and gelation phenomena. *SIAM J. Sci. Comput.*, 22:802–821, 2000.
- [11] Michael Goodson and Markus Kraft. An efficient stochastic algorithm for simulating nano-particle dynamics. *J. Comput. Phys.*, 183,:210–232, 2002.
- [12] R. McGraw. Description of aerosol dynamics by the quadrature method of moments. *Aerosol Sci. Technol.*, 27(2):255–265, 1997.
- [13] Daniel L. Marchisio, R. Dennis Vigil, and Rodney O. Fox. Quadrature method of moments for aggregation-breakage processes. *J. Colloid Interf. Sci.*, 258:322–334, 2003.
- [14] Daniele L. Marchisio and Rodney O. Fox. Solution of population balance equations using the direct quadrature method of moments. *J. Aerosol Sci.*, 36:43–73, 2005.
- [15] J. A. Shohat and J. D. Tamarkin. *The Problem of Moments*. American Mathematical Society, Providence, Rhode Island, revised edition, 1970.
- [16] Douglas L. Wright Jr. Numerical advection of moments of the particle size distribution in eulerian models. *J. Aerosol Sci.*, 38:352–369, 2007. doi: 10.1016/j.jaerosci.2006.11.011.
- [17] Antonio Attili and Fabrizio Bisetti. Application of a robust and efficient lagrangian particle scheme for the evolution of soot statistical moments in turbulent flames. *Comput. Fluids*, 2012. (submitted).
- [18] O. Desjardins, G. Blanquart, G. Balarac, and H. Pitsch. High order conservative finite difference scheme for variable density low Mach number turbulent flows. *J. Comput. Phys.*, 227(15):7125–7159, 2008.
- [19] J. Kim and P. Moin. Application of a fractional-step method to incompressible Navier-Stokes equations. *J. Comput. Phys.*, 59(2):308–323, 1985.
- [20] R. Falgout, J. Jones, and U. Yang. The design and implementation of hypre, a library of parallel high performance preconditioners. In Are Magnus Bruaset and Aslak Tveito, editors, *Numerical Solution of Partial Differential Equations on Parallel Computers*, pages 267–294. Springer, 2006.
- [21] M. A. Ofshanskii and V. M. Staroverov. On simulation of outflow boundary conditions in finite difference calculations for incompressible fluid. *Int. J. Numer. Methods Fluid*, 33(4):499–534, 2000.
- [22] X.-D. Liu, S. Osher, and T. Chan. Weighted essentially non-oscillatory schemes. *J. Comput. Phys.*, 115:200–212, 1994.
- [23] Steven L. Girshick and Chia Pin Chiu. Kinetic nucleation theory: A new expression for the rate of homogeneous nucleation from an ideal supersaturated vapor. *J. Chem. Phys.*, 93:1273–1277, 1990. doi: 10.1063/1.459191.
- [24] R. Becker and W. Döring. Kinetische Behandlung der Keimbildung in übersättigten Dämpfen. *Ann. Phys. (Leipzig)*, 24:719–752, 1935.

- [25] K. Okuyama, Y. Kousaka, D. R. Warren, R. C. Flagan, and J. H. Seinfeld. Homogeneous nucleation by continuous mixing of high-temperature vapor with room temperature gas. *Aerosol Sci. Technol.*, 6:15–27, 1987.
- [26] T. K. Lesniewski. *Particle nucleation and growth in turbulent jets*. PhD thesis, University of California, Los Angeles, 1997.
- [27] Kaarle Hämeri and Markku Kulmala. Homogeneous nucleation in a laminar flow diffusion chamber: The effect of temperature and carrier gas on dibutyl phthalate vapor nucleation rate at high supersaturations. *J. Chem. Phys.*, 105(17):7096–7704, 1996.
- [28] L. E. Reichl. *A Modern Course in Statistical Physics*. John Wiley & Son, New York, second edition, 1997.
- [29] S. K. Loyalka and J. W. Park. Aerosol growth by condensation: A generalization of Mason’s formula. *J. Colloid Interf. Sci.*, 125(2):712–716, 1988.
- [30] E. Hairer, S. P. Norsett, and G. Wanner. *Solving Ordinary Differential Equations I. Nonstiff Problems*. Springer Series in Computational Mathematics. Springer-Verlag, 2nd edition, 1993.
- [31] D.C. Haworth. Progress in probability density function methods for turbulent reacting flows. *Prog. Energy Combust. Sci.*, 36(2):168–259, 2010. doi: 10.1016/j.pecs.2009.09.003.
- [32] Petros Koumoutsakos. Multiscale flow simulations using particles. *Annu. Rev. Fluid Mech.*, 37:457–487, 2005.
- [33] I. F. Sbalzarini, J. H. Walther, M. Bergdorf, S. E. Hieber, E. M. Kotsalis, and P. Koumoutsakos. PPM—a highly efficient parallel particle–mesh library for the simulation of continuum systems. *J. Comput. Phys.*, 215(2):566–588, 2006.
- [34] P. Chatelain, A. Curioni, M. Bergdorf, D. Rossinelli, W. Andreoni, and P. Koumoutsakos. Billion vortex particle direct numerical simulations of aircraft wakes. *Comput. Meth. Appl. Mech. Engrg.*, 197:1296–1304, 2008. doi: 10.1016/j.cma.2007.11.016.
- [35] Antonio Attili and Fabrizio Bisetti. Statistics and scaling of turbulence in a spatially developing mixing layer at $Re_\lambda = 250$. *Phys. Fluids*, 24:035109, 2012. doi: 10.1063/1.3696302.
- [36] P. E. Dimotakis. Turbulent free shear layer mixing and combustion. *High Speed Flight Popul. Syst.*, 137:265–340, 1991.
- [37] T. K. Lesniewski and S. K. Friedlander. The effect of turbulence on rates of particle formation by homogeneous nucleation. *Aerosol Sci. Technol.*, 23:174–182, 1995. doi: 10.1080/02786829508965302.
- [38] J. Wu and S. Menon. Aerosol dynamics in the near field of engine exhaust plumes. *J. Appl. Meteorol.*, 40:795–809, 2001.
- [39] L. Falk and E. Schaer. A PDF modelling of precipitation reactors. *Chem. Eng. Sci.*, 56:2445–2457, 2001.
- [40] Kun Zhou and Tat Leung Chan. Simulation of homogeneous particle nucleation in a free turbulent jet. *Aerosol Sci. Technol.*, 45:973–987, 2011.